Robust Skin Attachable Sensor for Core Body Temperature Monitoring

Y. Tanaka, D. Matsunaga, T. Tajima, *Member, IEEE*, and M. Seyama

***Abstract*—We designed a skin-attachable sensor for measuring core body temperature (CBT). Past studies on non-invasive CBT measurement did not consider heat loss and measurement errors caused by ambient convection. To address the effect of convection, we designed a heat flow path in the structure of the CBT sensor. Topology optimization provided a systematic design procedure without the need for numerous, complex trials. By using topology optimization, we developed an optimized aluminum structure, a truncated cone with a hole. The sensor with the aluminum structure was evaluated by numerical calculation and experiment. We determined that the heat loss induced by ambient convection was effectively reduced, and the CBT estimation accuracy and robustness to convection were improved. The feasibility of the CBT sensor was demonstrated in an experiment using a phantom with an accuracy of 0.1 °C, showing potential for applications to thermal and fluidic devices.**

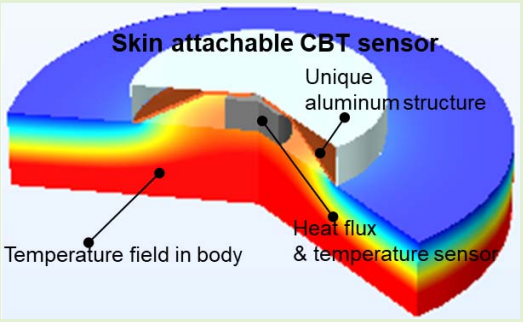

***Index Terms*—Topology optimization, core body temperature, non-invasive.**

I. Introduction

CORE body temperature (CBT) is the temperature of internal organs located deep within the body such as the rectum, esophagus, and brain. CBT fluctuates in roughly 24-hour cycles, and it is known to reflect circadian rhythms, i.e., the body's internal clock [2]. For instance, the CBT of a healthy person drops during sleep at night. A phase gap between one's biological clock and the social clock can affect sleep quality and exercise performance and can lead to serious health problems such as metabolic aberrations and depression [1]–[8].

CBT can be monitored over the course of a day to visualize and improve one's health conditions. Current CBT monitoring techniques measure esophageal, pulmonary, artery, and rectal temperature. Among these, rectal temperature is regarded as most reliable for monitoring circadian rhythm [5]. However, measuring rectal temperature requires a sensor to be inserted into the rectum, which may cause infection and damage to the rectal cavity. Skin-attachable, in-ear, and ingestible sensors have been studied as alternatives [9]–[17]. In-ear sensors require the user to be in a resting state, while ingestible sensors are limited in terms of monitoring duration and difficulty of sensor collection after use. We focus on skin-attachable sensors as they are more practical for daily use. There are two types of sensors; one uses an inbuilt heater to compensate for the gap between the skin and body temperatures (i.e., zero heat flux method) [11]. While this sensor is capable of monitoring CBT with high accuracy and traceability, the energy consumption of the heater limits its usage in hospitals. The second type is fully passive and does not require a heater, instead using a heat equivalent circuit as shown in Fig. 1 [12]–[14]. CBT is given by

$$T_{CBT} = T_{skin} + R_{sensor} H_{Body} \tag{1}$$

where T_{skin} is skin temperature, H_{Body} is the heat flux from the body's core, and R_{Sensor} is a coefficient related to the heat resistance of the sensor. $R_{\mathrm{Sensor}}$is a function of the sensor structure and size. Equation (1) assumes lossless heat transfer from the body core to the sensor. However, ambient convection extracts heat flux H_{Loss} (Fig. 1). Because ambient convection results in over or under estimation of the heat flux H_{Body}, the coefficient R_{Sensor}varies with the convection. The convection results in heat dissipation, where heat is carried passively by fluid motion initiated and maintained by external sources such as air conditioners or by activities such as jogging. Thus, a CBT sensor that can reduce heat loss is required for continuous CBT monitoring. In other words, the sensor should maintain the value of coefficient R_{Sensor} when the ambient convection changes. Previous studies assumed lossless heat transfer, and their proposed sensor structure focused only on

Manuscript received March 9, 2021; revised April 23, 2021; accepted April 23, 2021. Date of publication April 26, 2021; date of current version July 14, 2021. The associate editor coordinating the review of this article and approving it for publication was Dr. Ing. Emiliano Schena. *(Corresponding author: Y. Tanaka.)*

The authors are with NTT Device Technology Laboratories and the Bio-Medical Informatics Research Center, NTT Corporation, Kanagawa 243-0198, Japan (e-mail: tanaka.yujiro@lab.ntt.co.jp).

Digital Object Identifier 10.1109/JSEN.2021.3075864

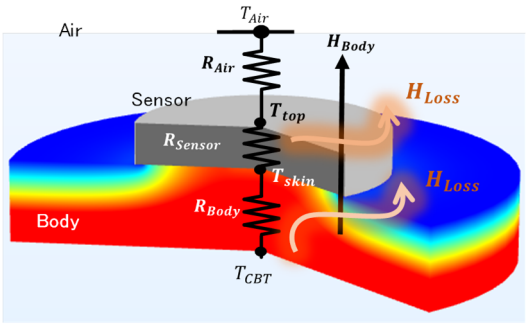

Fig. 1. CBT estimation using skin-attachable sensor. H_{Body} is heat flux from the body's core. H_{Loss} is induced by ambient convection.

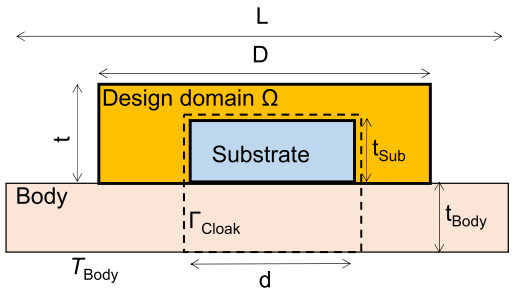

Fig. 2. Schematic cross section image of fabricated CBT sensor. The size of the heat resistance substrate and chassis are fixed. The aluminum structure is optimized in the design domain.

the depth direction to obtain the heat flux H_{Body}. As a result, the structure of these sensors is nearly uniform in the lateral direction and do not take heat loss into account [12]–[14].

We aimed to address this by designing the structure of a CBT sensor using topology optimization, which provides a systematic design procedure and has become widely used in various fields (e.g., thermo-fluid dynamics) [18]–[21]. Then we fabricated the CBT sensor and verified its effectiveness by both numerical calculation and experiment. The proposed CBT sensor was robust to ambient convection, making it possible to monitor CBT in daily life and visualize circadian rhythm.

II. Sensor Design

A schematic cross-sectional image of the CBT sensor is shown in Fig. 2. The CBT sensor has a cylindrical chassis with diameter $D = 30$ mm and height $t = 5$ mm, which were determined to be optimal for mobility and usability. The chassis contains a heat-resistant substrate and an aluminum structure in the design domain. The heat-resistant substrate is able to measure the heat flux.

The CBT sensor was assumed to be attached to the forehead and used during jogging. The wind speed V_{In} was assumed to be 5 m/s (at a jogging speed of 18 km/h). The depth of the sensor body, t_{Body}, was assumed to be 10 mm. To simplify optimization for the fluid and heat transfer interaction system, we utilized the heat transfer coefficient H at the boundary with ambient air to take convectional heat transfer into consideration. The relationship between the wind speed and heat transfer coefficient H was estimated by the Nusselt number Nu, Prandtl number Pr, and Reynolds number Re:

$$Nu = \frac{H t_{Body}}{\lambda_{Air}} \tag{2}$$

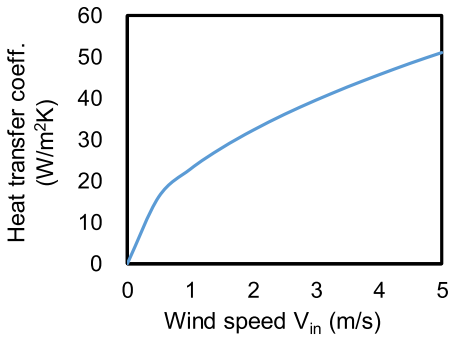

Fig. 3. Relationship between heat transfer coefficient and wind speed at characteristic length $L = 30$ mm.

$$Pr = \frac{C_{p_{Air}} \mu_{Air}}{\lambda_{Air}} \tag{3}$$

$$Re = \frac{\rho_{Air} V_{In} t_{Body}}{\mu_{Air}} \tag{4}$$

where V_{In} is wind speed, L is the characteristic length, ρ_{Air} is air density, μ_{Air} is air viscosity, and λ_{Air} is thermal conductivity. For laminar flow, the Nusselt number Nu is given by [22]

$$Nu = 0.664 Re^{\frac{1}{2}} Pr^{\frac{1}{3}} \tag{5}$$

Substituting (2), (3), and (4) into (5), we obtain the heat transfer coefficient as a function of wind speed V_{I} by.

$$H = 0.664 Pr^{1/3} \sqrt{\frac{\rho_{Air}}{\mu_{Air}}} \cdot \sqrt{\frac{V_{In}}{L}} \tag{6}$$

The relationship between heat transfer coefficient H and wind speed is shown in Fig. 3, in which the diameter of the CBT sensor is used as characteristic length L. The heat transfer coefficient ranges from 0 to 50 W/m^{2}K when V_{In} ranges from 0 to 5 m/s.

We designed the aluminum structure using topology optimization to reduce heat loss H_{Loss}. To minimize heat loss, we define the objective as the minimization of heat flux across boundary Γ_{Cloak} as

$$J = H_{Loss}, H_{\mathrm{Loss}} = \int_{\Gamma_{\mathrm{Cloak}}} H \mathrm{d}\Gamma$$

Boundary Γ_{Cloak} surrounds the heat-resistant substrate and the domain beneath it, as shown in Fig. 2. The objective's sensitivity to changes in the design variables were required for the optimization and was obtained by adjoint sensitivity analysis. The method of moving asymptotes (MMA) was used to calculate the optimization. The numerical computation was performed using COMSOL Multiphysics 5.5®. The parameters used in the optimization computation are shown in Table I.

$$\nabla \left(k_\gamma \nabla T\right) = 0 \tag{7}$$

The thermal conductivity distribution of the material was optimized using a spatially defined density design variable γ. The thermal conductivity k_γ is interpolated by

$$k_\gamma = k_{Al} + (k_{Air} - k_{Al})\, \gamma \frac{1+q}{\gamma + q} \tag{8}$$

TABLE I
COMPUTATION PARAMETERS

Variable	Variable	Value
Sensor height	t	5 mm
Sensor diameter	D	30 mm
Substrate height	t_{Sub}	4 mm
Substrate diameter	d	8 mm
Body depth	t_{Body}	10 mm
Ambient temp.	T_{in}	20 °C
CBT	T_{Body}	37 °C
Wind speed	V_{In}	5 m/s
Calculation diameter	L	80 mm

where k is thermal conductivity (the subscript indicates the material; e.g., k_{al}: conductivity of aluminum), γ is the design variable moving from 0 to 1, and q is a parameter related to the nonlinearity of interpolation. As q decreases, the nonlinearity increases. The thermophysical parameters used in the numerical calculation are shown in Table II. A typical problem that arises in topology optimization is a gray scale of material distribution, which means a porous structure and lower fabrication tolerance. To avoid this, we used a Helmholtz PDE filter,

$$\gamma_f = \gamma + R_{min}^2 \nabla \gamma_f \tag{9}$$

and smoothed Heaviside projection [18],

$$\gamma = \frac{\tanh\left(\beta\left(\gamma_f - \theta_\beta\right)\right) + \tanh\left(\beta\theta_\beta\right)}{\tanh\left(\beta\left(1 - \theta_\beta\right)\right) + \tanh\left(\beta\theta_\beta\right)} \tag{10}$$

where β is a parameter determining the steepness of projection and θ_β is the threshold parameter. The threshold parameter is fixed at 0.5. In this work, parameter β was 15, and the initial design variable was 0.5.

The resulting optimized CBT sensor is shown in Fig. 4(a). The red area is the optimized aluminum structure which resembles a truncated cone with a hole at the top. The complex curves and inconsistent thickness make fabrication difficult and decreases the fidelity of numerical calculation. To improve the fidelity of the structure and fabrication tolerance, we simplified the structure so that it has a uniform thickness of 0.5 mm and a smooth surface as shown in Fig. 4(b), thus optimizing the aluminum structure. The diameter of the hole in the truncated cone is 2 mm. The relationship between the diameter of the table and hole of the truncated cone, and the estimation error are show in Fig. 4 (c). The estimation error were calculated numerically for evaluation. The estimation was performed under the wind speed condition $V = 5$ m/s. The coefficient for estimating CBT, R_{Sensor}, was obtained with T_{skin} and H_{Body} at wind speed $V = 1$ m/s. The estimation error is gradually decayed with decrease of the table diameter D, or decrease of the hole diameter d and bottom out at approximately 2 mm. For the simplified optimized structure (Fig. 4 (b)), heat loss and estimation error depending on wind speed were calculated as shown in Fig. 5 (a, b). The blue and orange plots indicate the resulting calculations with and without the aluminum structure, respectively. The heat loss H_{Loss} and the estimation error increased with wind speed V_{In} with or without the aluminum structure, though

TABLE II
THERMO AND FLUIDIC PHYSICAL PARAMETERS

Part	Thermal conductivity k (W/mK)
Air	0.02
Body	0.37
Aluminum	204

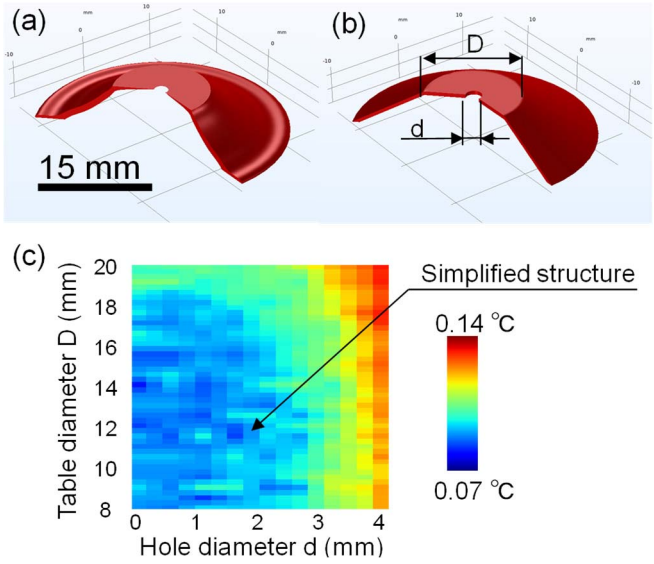

Fig. 4. (a) Optimized CBT sensor structure without chassis. (b) Schematic image of simplified structure. (c) Relationship between hole diameter d, table diameter D, and estimation error.

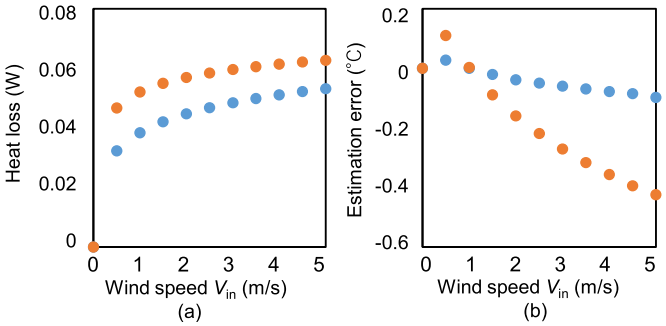

Fig. 5. Comparison of heat loss and estimation error with (blue) and without (orange) optimized aluminum structure. (a) Heat loss vs wind speed V_{in}. (b) Estimation error vs wind speed V_{in}.

they were effectively reduced by the structure compared with when the structure was not used. The maximum estimation errors with and without the optimized aluminum structure were 0.1 and 0.4°, respectively, at wind speed $V_{\mathrm{in}} = 5$ m/s.

III. EXPERIMENTAL

The CBT sensor was fabricated as shown in Fig. 6 (a) and (b). The truncated cone was made of aluminum. The thickness was 0.5 mm across the entire structure. The height was 5 mm, and the diameter of the hole in the truncated cone was 2 mm. The heat-resistant substrate was made of polylactic acid (PLA). The diameter and height the CBT sensor chassis were 31 and 5.1 mm, respectively. The top and bottom of the chassis was made

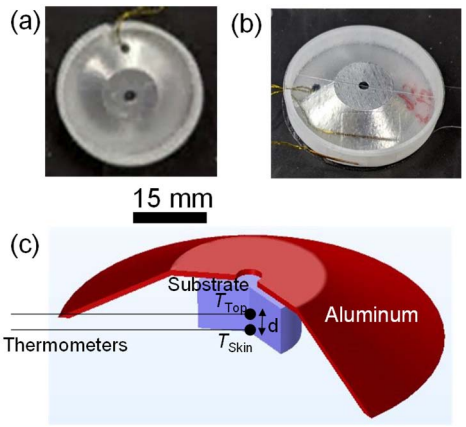

Fig. 6. Photograph of fabricated CBT sensor. (a) Top view. (b) Bird's eye view. (c) Schematic cross-sectional image of CBT sensor. Two thermometers inserted in the hole on the side of the aluminum structure were integrated with the substrate with a gap of d. The height, the diameter and weight of the CBT sensor were 5 mm, 30 mm, and approximately 3 g, respectively.

of 0.1-mm thick polyethylene terephthalate (PET), and the side was made of 0.5-m thick PLA. Two platinum resistance thermometers inserted in the hole in the side of the truncated cone were integrated with the heat-resistant substrate. The gap between the two thermometers was 2 mm (Fig. 6(c)). The diameter and length of each thermometer were 0.4 and 1 mm, respectively. The temperature of the hotplate, $T_{Hotplate}$, was measured every 1 s with a thermometer (MC-0401, Netsushin, Japan). The temperature was read out from the thermometer by a data logger (NX3100, Netsushin, Japan). The coefficient R_{Sensor} was estimated from the temperatures T_{skin} and T_{top} taken by the two thermometers. The heat flux H_{Body} was proportional to the temperature gap T_{skin}-T_{top}:

$$H_{Body} \propto T_{Skin} - T_{Top} \tag{11}$$

Substituting (11) into (1), we obtain coefficient R_{Sensor} using the hotplate temperature at a specific time:

$$R_{sensor} = \frac{T_{Hotplate} - T_{Skin}}{T_{Skin} - T_{Top}} \tag{12}$$

EPDM rubber with a thickness of 10 mm was used as a phantom as it has thermal conductivity k similar to that of the human body. The phantom was placed on the hotplate, and the sensor was set on the phantom. The ambient temperature was room temperature (20°). Convection was induced by a fan placed above the CBT sensor. The wind speed above the CBT sensor was measured with a hot-wire anemometer.

IV. Results and Discussion

Fig. 8 shows a comparison between the hotplate and estimated temperatures when the temperature of the hotplate $T_{\mathrm{Hotoplate}}$ and wind speed V_{In} ranged from 32 to 42° and 0 to 5 m/s, respectively. Coefficient R_{Sensor} was 2.45 in the experiment, whereas it was 2.5 in the computation. This discrepancy in the coefficient R_{Sensor} may have been due to the contact heat resistance between the sensor and phantom and the size of the thermometers. The raw estimation temperature is indicated

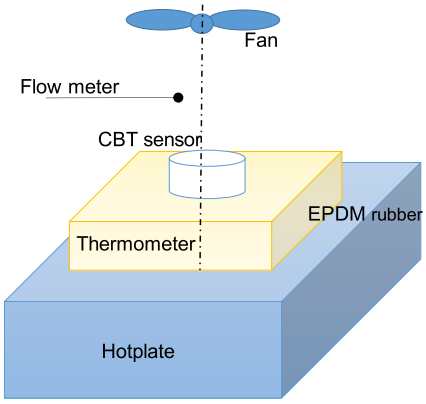

Fig. 7. Experimental configuration. The hotplate simulated CBT. The CBT sensor was set on the phantom (EPDM rubber) placed on the hotplate. Convection was induced by a fan above the CBT sensor, and the wind speed V_{in} was monitored by a flow meter.

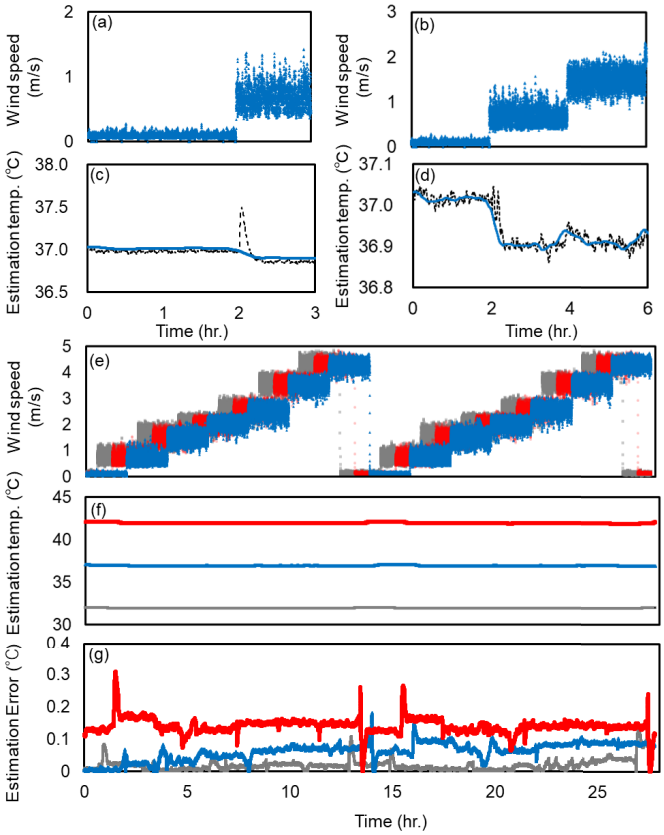

Fig. 8. Wind speed dependence of estimation temperature and error. (a) and (b) are magnified images of wind speed profile. (c) Raw and compensated estimated temperatures at wind profile in (a). Raw and compensated estimated temperatures are indicated by dotted and solid lines, respectively. (d) Compensated and 8-min moving averaged estimated temperatures at wind profile in (b). Compensated and averaged estimated temperatures are indicated by dotted and solid lines, respectively. (e) Wind speed profile for the entire duration of experiment. (f) and (g) are estimated temperatures and errors at the wind profile in (e). Gray, blue, and red plots in (e) to (g) are the hotplate temperatures set at 32, 37, 42°C, respectively.

by the dotted line in Fig. 8 (c). A transient overshoot can be observed immediately after the wind speed changes, and then the temperature becomes steady. The overshoot was caused by the difference in the time constant of heat transfer in the

body and the sensor. While the temperature of the sensor changed quickly in response to the wind speed, the body temperature required more time due to its large heat capacity. The difference resulted in the transient overestimation of heat flux H_{Body}. To compensate for the transient overshoot $T_{\mathrm{over\_est}}$, we estimate it by deriving from the overestimation of the heat flux using the equation below:

$$T_{Over\_est} \sim A\mathrm{erfc}\left(\frac{B}{\sqrt{t}}\right) - C\sqrt{t}\exp\left(-\frac{1}{\sqrt{t}}\right) \tag{13}$$

where, A, B, and C are constant parameters and t is the elapsed time from the start of the overshoot. We determine the overestimated region by using the standard deviation of estimated temperature σ in 5 min. If the estimated temperature exceeds 3 σ, we regard it as overshoot and obtain A, B, and C by fitting Eq. (13) to the raw estimation temperature. The solid line in Fig. 8(c) represents a typical compensated result, though sharp noise still remained as shown in Fig. 8(d). To denoise the results, we conducted averaging for 8 min. The wind speed, estimated temperature with compensation and averaging, and estimation error profile for 29 hours are shown in Fig. 8(e, f, g, respectively). The wind speed ranged from about 0 to 5 m/s, and the reference hotplate temperatures were set at 32, 37, and 42°. The estimation error became large when the wind speed changed from 0 to 1 m/s and from 5 to 0 m/s. There is a large gap between the heat transfer effect of conduction and convection, which results in a large error. Without these transient errors, the effects of the wind are successfully reduced. In terms of reference hotplate temperature, the systematic error can be seen in Fig. 8(g), in which the error at the hotplate temperature of 42° is consistently 0.1°. The relationship between hotplate temperature and estimation error is shown Fig. 9(a). The estimated temperature showed a linear response against the hotplate temperature, and the estimation error was 0.1°. The estimation error was assessed by comparing the estimated temperature $T_{\mathrm{Estimation}}$ to the reference hotplate temperature, T_{Hotplate}, using root mean square error (RMSE) as follows:

$$\mathrm{RSME} = \sqrt{\frac{1}{n}\sum_{i=1}^{n}\left(T_{Estimation} - T_{Hotplate}\right)^2} \tag{14}$$

The estimation error at each hotplate temperature is shown in Fig. 9(b). The amplitude of CBT is about 1° [23], which shows that the proposed CBT sensor can be used to monitor CBT over the course of a day. The systematic error can be found in this figure as well, which increases with the hotplate temperature. Although systematic errors may arise depending on the reference temperature, the proposed structure successfully decreased the effect of the wind. Removing the systematic error should be feasible by signal processing. This work assumes that the thermal properties of the body are steady; however, changes in blood flow during exercise affects these properties to some extent. Combining the developed sensor with additional CBT sensors or external heart rate sensors should be effective for estimating the effects.

Lastly, we discuss the analogy of heat loss reduction with the optimized aluminum structure, the truncated cone with a hole. A schematic image of heat flow around the CBT sensor is shown in Fig. 10(a). Heat flux H_{Body} comes from the body core, and the estimation error was induced by heat loss H_{Loss}. However, the aluminum structure collects heat H_{Plus} from the surrounding region of the CBT sensor. The collected heat is now isolated from the heat flux since the foot of the truncated cone structure is far enough from the heat-resistant substrate. Collected heat H_{Plus} increases the temperature of region surrounding the heat-resistant substrate, and it blocks heat loss H_{Loss}. Additionally, the hole in the truncated cone of the aluminum structure enables heat flux H_{Body} to be easily released into ambient air. The numerically calculated temperature fields with and without the aluminum structure are shown in Fig. 10(b) and (c). As shown, the temperature surrounding the heat-resistant substrate is increased compared with that without the aluminum structure. The heat equivalent circuit is shown in Fig. 10(b).

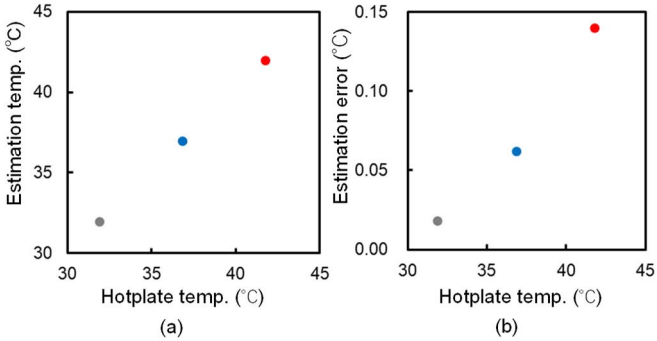

Fig. 9. Comparison between ref erence hotplate and estimated temperatures. (a) Estimation error vs hotplate temperature. (b) Estimation error vs wind speed *V*. Gray, blue, and red plots in (e) to (g) are the hotplate temperature set at 32, 37, 42°C, respectively.

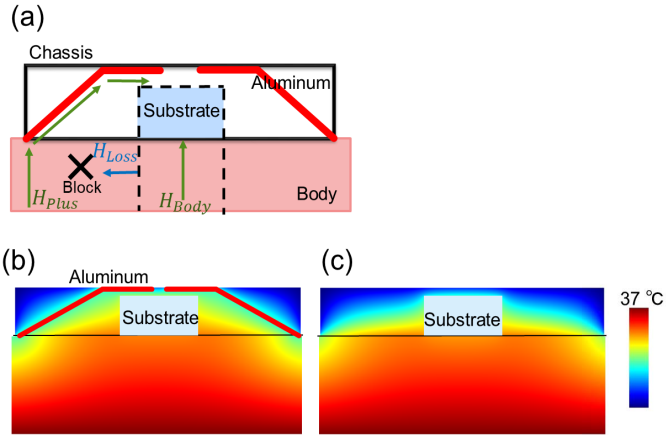

Fig. 10. Analogy of heat loss reduction with optimized aluminum structure. (a) Schematic illustration of heat flow on temperature field. (b, c) Temperature field with and without the optimized aluminum structure. The distance between the skin and the body core is 10 mm.

V. Conclusion

We designed a skin-attachable CBT sensor that accounts for the heat loss caused by ambient convection during everyday activities. The aluminum structure of the CBT sensor—a truncated cone with a hole—effectively reduced heat loss. The structure was designed using topology optimization and then

simplified so that it had no complex curves, a smooth surface, and uniform thickness to improve fabrication tolerance. The simplification of the structure was verified via numerical calculation. The optimized CBT sensor was fabricated and successfully demonstrated in an in-vitro experiment using an EPDM rubber phantom with an accuracy of 0.1°. Ambient convection was provided by a fan with wind speed ranging from 0 to 5 m/s. Continuous CBT monitoring over the course of a day is feasible with the develop "be applied to the dual heat flux and zero heat flux methods.

REFERENCES

[1] W. E. Scales, A. J. Vander, M. B. Brown, and M. J. Kluger, "Human circadian rhythms in temperature, trace metals, and blood variables," *J. Appl. Physiol.*, vol. 65, no. 4, pp. 1840–1846, Oct. 1988.

[2] G. Costa, "The impact of shift and night work on health," *Appl. Ergonom.*, vol. 27, no. 1, pp. 9–16, Feb. 1996.

[3] J. E. Gangwisch *et al.*, "Short sleep duration as a risk factor for hypertension: Analyses of the first," *Nat. Health Nutrition Examination Survey. Hypertension*, vol. 47, no. 5, pp. 833–839, 2006.

[4] S. Hashimoto, K. Nakamura, S. Honma, H. Tokura, and K. Honma, "Melatonin rhythm is not shifted by lights that suppress nocturnal melatonin in humans under entrainment," *Amer. J. Physiol.-Regulatory, Integrative Comparative Physiol.*, vol. 270, no. 5, pp. R1073–R1077, May 1996.

[5] F. Lévi, A. Okyar, S. Dulong, P. F. Innominato, and J. Clairambault, "Circadian timing in cancer treatments," *Annu. Rev. Pharmacol. Toxicol.*, vol. 50, no. 1, pp. 377–421, Feb. 2010.

[6] S. Higuchi, Y. Motohashi, Y. Liu, M. Ahara, and Y. Kaneko, "Effects of VDT tasks with a bright display at night on melatonin, core temperature, heart rate, and sleepiness," *J. Appl. Physiol.*, vol. 94, no. 5, pp. 1773–1776, May 2003.

[7] N. N. Takasu *et al.*, "Repeated exposures to daytime bright light increase nocturnal melatonin rise and maintain circadian phase in young subjects under fixed sleep schedule," *Amer. J. Physiology-Regulatory, Integrative Comparative Physiol.*, vol. 291, no. 6, pp. R1799–R1807, Dec. 2006.

[8] G. Jean-Louis, D. F. Kripke, R. J. Cole, and J. A. Elliott, "No melatonin suppression by illumination of popliteal fossae or eyelids," *J. Biol. Rhythms*, vol. 15, no. 3, pp. 265–269, Jun. 2000.

[9] T. Nemoto and T. Togawa, "Improved probe for a deep body thermometer," *Med. Biol. Eng. Comput.*, vol. 26, no. 4, pp. 456–459, Jul. 1988.

[10] K.-I. Kitamura, X. Zhu, W. Chen, and T. Nemoto, "Development of a new method for the noninvasive measurement of deep body temperature without a heater," *Med. Eng. Phys.*, vol. 32, no. 1, pp. 1–6, Jan. 2010.

[11] M. Yamakage and A. Namiki, "Deep temperature monitoring using a zero-heat-flow method," *J. Anesthesia*, vol. 17, no. 2, pp. 108–115, May 2003.

[12] R. H. Fox, A. J. Solman, R. Isaacs, A. J. Fry, and I. C. MacDonald, "A new method for monitoring deep body temperature from the skin surface," *Clin. Sci. Mol. Med.*, vol. 44, no. 1, pp. 81–86, 1973.

[13] Y. Zhang *et al.*, "Theoretical and experimental studies of epidermal heat flux sensors for measurements of core body temperature," *Adv. Healthcare Mater.*, vol. 5, no. 1, pp. 119–127, Jan. 2016.

[14] M. Huang, T. Tamura, Z. Tang, W. Chen, and S. Kanaya, "A wearable thermometry for core body temperature measurement and its experimental verification," *IEEE J. Biomed. Health Informat.*, vol. 21, no. 3, pp. 708–714, May 2017.

[15] S. Yoshida, H. Miyaguchi, and T. Nakamura, "Development of tablet-shaped ingestible core-body thermometer powered by gastric acid battery," *IEEE Sensors J.*, vol. 18, no. 23, pp. 9755–9762, Dec. 2018.

[16] K. Kalantar-zadeh, N. Ha, J. Z. Ou, and K. J. Berean, "Ingestible sensors," *ACS Sensors*, vol. 2, no. 4, pp. 468–483, Apr. 2017.

[17] C. Byrne and C. L. Lim, "The ingestible telemetric body core temperature sensor: A review of validity and exercise applications," *Brit. J. Sports Med.*, vol. 41, no. 3, pp. 126–133, Mar. 2007.

[18] G. H. Yoon, "Topological design of heat dissipating structure with forced convective heat transfer," *J. Mech. Sci. Technol.*, vol. 24, no. 6, pp. 1225–1233, Jun. 2010.

[19] B. S. Lazarov, M. Schevenels, and O. Sigmund, "Topology optimization considering material and geometric uncertainties using stochastic collocation methods," *Struct. Multidisciplinary Optim.*, vol. 46, no. 4, pp. 597–612, Oct. 2012.

[20] F. Wang, B. S. Lazarov, and O. Sigmund, "On projection methods, convergence and robust formulations in topology optimization," *Struct. Multidisciplinary Optim.*, vol. 43, no. 6, pp. 767–784, Jun. 2011.

[21] O. Sigmund and K. Maute, "Topology optimization approaches," *Struct. Multidisciplinary Optim.*, vol. 48, no. 6, pp. 1031–1055, Dec. 2013.

[22] *Incropera's Principles of Heat and Mass Transfer*, Wiley, Hoboken, NJ, USA, 2017, pp. 405–407.

[23] R. Refinetti and M. Menaker, "The circadian rhythm of body temperature," *Physiol. Behav.*, vol. 51, no. 3, pp. 613–637, Mar. 1992.

Y. Tanaka received the B.S. and M.S. degrees in engineering from Tohoku University, in 2011 and 2013, respectively. In 2013, he joined NTT Microsystem Integration Laboratories. Since 2014, he has been with NTT Device Technology Laboratories and the Bio-Medical Informatics Research Center, where he is currently studying photo-acoustic technology for bio-sensing. He is a member of the Japan Society of Applied Physics.

D. Matsunaga received the B.S. and M.S. degrees in engineering from Kobe University, Japan, in 2015 and 2017, respectively. In 2017, he joined NTT Device Technology Laboratories, Japan. Since 2019, he has been with the NTT Bio-Medical Informatics Research Center, where he is currently studying heat transfer technology for bio-sensing. He is a member of the Institute of Electronics, Information and Communication Engineers, Japan.

T. Tajima (Member, IEEE) received the B.S. and M.E. degrees from the University of Tokyo, Tokyo, Japan, in 2000 and 2002, respectively, and the Ph.D. degree from the Tokyo Institute of Technology in 2017. In 2002, he joined Telecommunication Energy Laboratories, Nippon Telegraph and Telephone Corporation (NTT), Japan, where he has been engaged in the research and development of laser photo-acoustic spectroscopy for biomedical sensing, sub-terahertz antenna in packages using SIW technology, and broadband dielectric spectroscopic systems using photonic integration technologies. He is currently a Senior Research Engineer with NTT Device Technology Laboratories and the Bio-Medical Informatics Research Center. His current research interests include multimodal biomedical analysis using millimeter waves, terahertz waves, optics, and ultrasonics. He is a member of the Institute of Electronics, Information and Communication Engineers and the Japan Society of Applied Physics.

M. Seyama received the B.S., M.E., and Ph.D. degrees from Waseda University, Tokyo, Japan, in 1995, 1997, and 2004, respectively. In 1997, she joined Nippon Telegraph and Telephone (NTT) and worked on an odor sensing system based on a plasma-polymerized organic film for environmental contamination and biogas, and a 1D surface plasmon resonance biosensor combined with a microfluidic device for on-site immunological sensing. She is currently a Senior Research Engineer and a Supervisor with NTT Device Technology Laboratories, Japan. Her current research interests include development of bio-sensing platforms for blood components and blood coagulation, including both invasive and noninvasive technologies. She is a member of the Japan Society of Applied Physics, the Electrochemical Society of Japan, and the American Chemical Society.